Appendix

Appendix A

The Detailed Description of Operator $\mathbf{G}_\omega$

The $\mathbf{G}_\omega$ is an operator that re-arranges pixels along a candidate geometrical directions [1]. All the candidate geometric directions are pre-defined in a patch and are uniformly partitioned in the interval [0, 2π]. The candidate directions are marked with the white lines shown in Fig. 1(a) and only 14 directions are presented as an illustrative example. The angle between the direction lines (red color in Fig. 1(b)) and the horizontal direction (dashed line in Fig. 1(b)) stands for these directions. Let the candidate directions be $\{\theta_1, \theta_2, \cdots, \theta_Q\}$ and a specified direction be $\theta_d \in \{\theta_1, \theta_2, \cdots, \theta_Q\}$, there is an associated direction line L_{θ_d} (red color in Fig. 1(b)) and its orthogonal line $L_{\theta_d}^{\perp}$ (blue color in Fig. 1(b)). Each patch pixel $x(r_X, r_Y)$ located at (r_X, r_Y) is orthogonally projected onto the line $L_{\theta_d}^{\perp}$ to get a new point $x(r_{\theta_d}^{\perp})$, and pixels are reordered by the projected distance along the line $L_{\theta_d}^{\perp}$. Finally, 64 pixels are used to produce a 1D column vector according to the order marked on each pixel in Fig. 1(c).

By rotating the central line in a 8×8 patch, 71 is the maximal number that determines discrete grids to cover the pixels. This setting allows maximally explore the geometric directions in a patch. As the default parameter setting in PBDW [1], 71 directions are pre-defined for 8×8 patches. We choose 71 directions in FDLCP in order to have a fair comparison to PBDW.

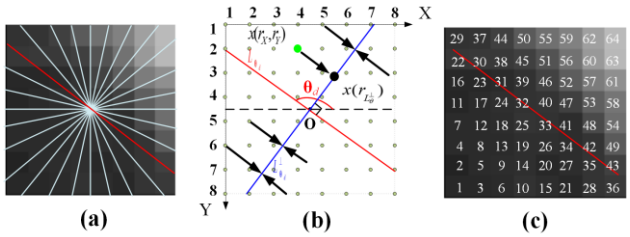

Fig. 1. Illustration of reordering pixels. (a) All candidate directions in a patch; (b) Projecting a pixel to the axis that is orthogonal to a given direction line L_{θ_d} associated with an angle θ_d; (c) indexes of reordering pixels into 1D vector.

Appendix B

Image Reconstructions Using Different Sparsifying Dictionaries/Transforms

We compare our proposed reconstruction method with that using Curvelets [2] or Contourlets [3, 4] as the sparsifying transform in CS-MRI. We directly utilize these transforms to reconstruct MR image. A better reconstructed image implies the dictionary/transform achieves the sparser representation.

The reconstruction model is

$$\min_{\mathbf{x}} \|\mathbf{\Psi x}\|_1 \quad s.t. \quad \|\mathbf{y} - \mathbf{F}_U\mathbf{x}\|_2 \le \varepsilon \qquad \text{(A1)}$$

where $\mathbf{\Psi}$ is the Curvelets or Contourlets transform. We use the public implementations of these two transforms [4, 5] shared by the respective authors. In the implementation, ADMM [6, 7] is adopted as the numerical algorithm to solve (A1). For Contourlets, we set 2^5, 2^4, 2^4, 2^3 directional sub-bands from coarse to fine scales, and employ the quincunx-type filter named pkva [8] and no downsampling of the low-pass sub-band at the first level decomposition. For Curvelets, we use wrapping-based fast discrete curvelets transform [5] with 5 decomposition levels and 16 angles at the 2nd coarsest level. Parameters in the reconstruction are tuned to obtain the optimal performance of each transform. Reconstructed images in Fig. 2 show that the proposed FDLCP achieves better image quality than Curvelets and Contourlets.

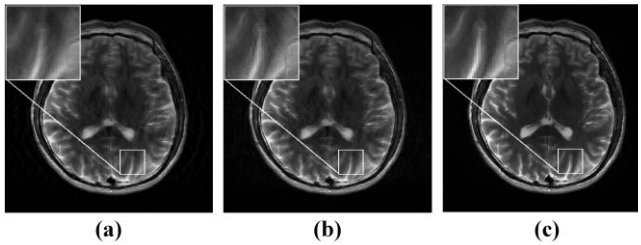

Fig. 2. Reconstructed images using different sparsifying transforms. (a-c) are reconstructed images using Curvelets, Contourlets, and the proposed FDLCP. The reconstruction errors, RLNE, of (a-c) are 0.1634, 0.1589 and 0.0935, respectively. The preserved structure similarity, SSIM, of (a-c) are 0.8407, 0.8572 and 0.9626, respectively. FDLCP achieves best results.

Appendix C

The FDLCP Using L_0 Norm Penalty in Reconstruction

The reconstruction model of FDLCP using the l_0 norm is

$$\min_{\mathbf{x}} \|\mathbf{\Phi x}\|_0 \quad s.t. \quad \|\mathbf{y} - \mathbf{F}_U\mathbf{x}\|_2 \le \varepsilon . \qquad \text{(A2)}$$

We also use the ADMM [6, 7] to solve the model. The whole process is the same as the Algorithm 2 except the thresholding. The sparse coefficients is obtained by hard thresholding and the threshold is $\sqrt{2/\beta}$ instead. The solution can be expressed as following

$$\boldsymbol{\alpha}^{(n+1)} = H_{\sqrt{2/\beta}}\left(\mathbf{\Phi x}^{(n+1)} - \mathbf{d}^{(n)}\right) \qquad \text{(A3)}$$

The l_0 norm penalty improves image quality (Fig. 3). The reconstruction error has been reduced by 22%. Although it is hard to prove the convergence theoretically, the curves in Fig. 4 empirically show that RLNE and the objective function in (A2) decreases and gradually stabilizes as the iteration times increase, although there is a small oscillation at the beginning.

The code of the FDLCP with both l_1 and l_0 norm minimization will be released at the authors' website [9].

APPENDIX D

EFFECT OF THE NUMBER OF DICTIONARY ATOMS IN DLMRI

In this appendix, as the reviewer requested, we add a comparison when the total number of dictionary atoms in DLMRI [10] is set the same as that in the proposed FDLCP, and analyze the effect of the number of dictionary atoms in DLMRI.

For the brain image shown in Fig. 3(a), there are actually 58 different geometrical directions estimated from all the brain image patches, other 13 directions are not found although 71 geometrical directions are typically predefined for a 8×8 patch in FDLCP. Therefore, the total number of atoms in FDLCP and DLMRI is 58×64=3712. The reconstructed images shown in Fig. 5 indicate that FDLCP preserves image edges better than DLMRI and achieve both lower RLNE and higher SSIM. Besides, FDLCP runs much faster (approximately 60s) than DLMRI.

Fig. 5(e-f) show that increasing the number of dictionary atoms in DLMRI can improve the reconstruction but also introduce more computations. When the number of dictionary atoms increases from 1024 to 4096, the improvements on RLNE and SSIM are marginal but the computation time is about 3.5 times. Taking the computation time into account, the number of dictionary atoms is set to 64. The original authors of DLMRI typically set the number of atoms being equal to the number of pixels in a patch [10], which leads to promising results both in their and our experiments.

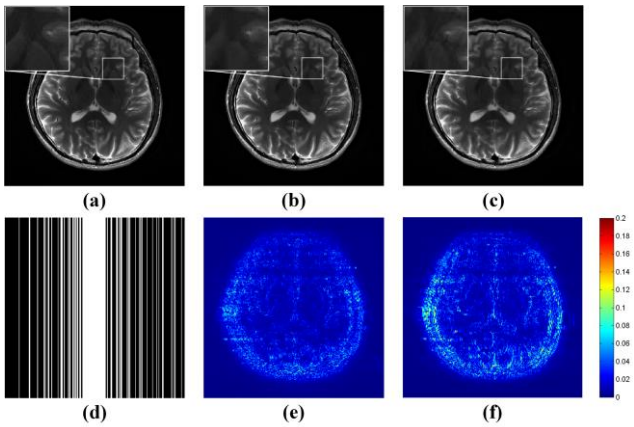

Fig. 3. A comparison of reconstruction images using l_0 and l_1 norm penalty in FDLCP. (a) A full sampled brain image; (b-c) Reconstructed images using l_0 and l_1 norm penalties, respectively; (d) Cartesian undersampling pattern with 32% data; (e-f) the reconstruction error magnitudes corresponding to (b-c), respectively; RLNE of (b-c) are 0.0741 and 0.0935, SSIM of (b-c) are 0.9707, 0.9626. Note: The parameters of FDLCP are the patch size 8×8, the pre-defined 71 different geometric directions for patch classification, the regularization parameter λ=10^3, and the times of updating reference image T=1.

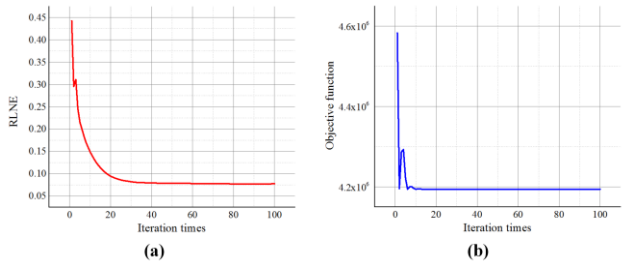

Fig. 4. Empirical convergence of the l_0 norm minimization problem. (a) The RLNE between the reconstructed image and the ground truth image versus the iteration time; (b) The values of the objective function in (A2) versus the iteration time.

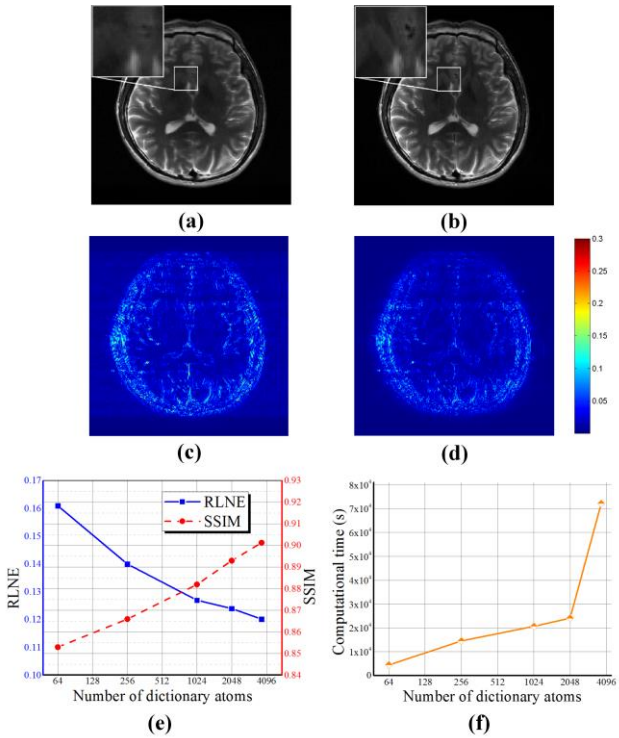

Fig. 5. The effect of the number of dictionary atoms in DLMRI. (a-b) are the reconstructed images using DLMRI and FDLCP when the total number of atoms is set as 3712; (c-d) are reconstruction error magnitudes corresponding to (a-b), respectively; RLNE of (a-b) are 0.1202 and 0.0935, SSIM of (a-b) are 0.9013, 0.9626; (e) RLNE and SSIM versus the number of dictionary atoms with comparison to FDLCP; (f) Computation time versus the number of dictionary atoms.

REFERENCES

[1] X. Qu et al., "Undersampled MRI reconstruction with patch-based directional wavelets," *Magn. Reson. Imaging*, vol. 30, pp. 964-977, Sep. 2012.

[2] E. Candès et al., "Fast discrete curvelet transforms," *Multiscale Model. Simul.*, vol. 5, pp. 861-899, Sep. 2006.

[3] M. N. Do and M. Vetterli, "The contourlet transform: An efficient directional multiresolution image representation," *IEEE Trans. Image Process.*, vol. 14, pp. 2091-2106, Dec. 2005.

[4] X. Qu et al., "Iterative thresholding compressed sensing MRI based on contourlet transform," *Inverse Probl. Sci. Eng.*, vol. 18, pp. 737-758, Aug. 2010.

[5] E. Candes et al. (2008). CurveLab toolbox. [Online]. Avaliable: http://www.curvelet.org/, 2008.

[6] S. Boyd et al., "Distributed optimization and statistical learning via the alternating direction method of multipliers," *Foundations and Trends® in Machine Learning*, vol. 3, pp. 1-122, Jan. 2011.

[7] Y. Liu et al. "Balanced sparse model for tight frames in compressed sensing magnetic resonance imaging," *PLoS ONE*. Apr. 2015. DOI: 1371/journal.pone.0119584

[8] P. See-May et al., "A new class of two-channel biorthogonal filter banks and wavelet bases," *IEEE Trans. Signal Process.*, vol. 43, pp. 649-665, Mar. 1995.

[9] X. Qu's website: http://www.quxiaobo.org

[10] S. Ravishankar and Y. Bresler, "MR image reconstruction from highly undersampled k-space data by dictionary learning," *IEEE Trans. Med. Imaging*, vol. 30, pp. 1028-1041, May. 2011.